

NUMERICAL INVESTIGATION INTO THE EFFECT OF SEPARATION AND STALL ON AEROFOIL NOISE

Jacob M. Turner

Aerodynamics & Flight Mechanics Research Group
 University of Southampton
 Highfield campus, Southampton, SO17 1BJ, UK
 J.M.Turner@soton.ac.uk

Jae-Wook Kim

Aerodynamics & Flight Mechanics Research Group
 University of Southampton
 Highfield campus, Southampton, SO17 1BJ, UK
 J.W.Kim@soton.ac.uk

ABSTRACT

Numerical simulations of a NACA0012 aerofoil at $Re_\infty = 50,000$ and $M_\infty = 0.4$ are presented at various angles of attack in order to invest the noise generated by separation and stall. Three cases are considered, low angle of attack laminar separation bubble (LSB), onset of stall, and deep stall. The primary aims of the work is to extend the current understanding of noise generation mechanisms in separated and stalled flows, and to contribute to a high fidelity database on aerofoil noise.

INTRODUCTION

Currently the majority of our understanding concerning aerofoil noise generation mechanisms is restricted to low angle of attack scenarios. Despite this, in a significant number of real applications (e.g. aero-engine components, high lift devices and wind farms) aerofoils are operated at high angles in order to maximise aerodynamic efficiency. Under these conditions aerofoils are highly susceptible to flow separation and stall, particularly if subjected to unsteady inflow conditions.

The high angle regime is characterised by significantly increased noise levels relative to attached flow cases. Depending on the angle of attack and Reynolds number various flow features may be responsible for the noise generation. This could include coherent leading edge vortex shedding, shear layer flapping, or shear layer instabilities (Lacagnina *et al.*, 2018). The stall noise generated by a NACA0012 aerofoil at $Re_\infty = 150,000$ and low speed ($U_\infty = 20\text{m/s}$ to 33m/s) has been investigated both experimentally and numerically by Moreau *et al.* (2009). They categorised the stall noise into two regimes, light stall and deep stall. In both cases the noise generated was found to be dipolar, and significantly increased at low frequencies relative to an attached flow case. In the deep stall regime strong tones were also present which were theorised to be caused by shear layer instabilities and vortex shedding.

It is also anticipated that the Mach number (M_∞) will play a significant role in the generation of stall noise. Wolf

et al. (2012), carried out a numerical study of a NACA0012 aerofoil at $Re_\infty = 408,000$, $M_\infty = 0.115$ and 0.4 at 5° angle of attack. It was demonstrated how at larger Mach numbers quadrupole sources (which are often neglected for aerofoil noise) become significant for medium to high frequencies.

The objective of the current work is to contribute to the understanding of the noise generation mechanisms associated with aerofoil stall and separation (in light of the large parameter space highlighted by previous findings). This study is part of a wider collaborative project between the University of Bristol and University of Southampton. The overall aim is to establish a comprehensive freely available data base of high quality numerical and experimental aerofoil noise data. The current paper considers the numerical results obtained to date, which are still a work in progress. High order accurate Navier-Stokes simulations are carried out for a NACA0012 aerofoil at three angles of attack 5° , 10° , and 15° , $Re_\infty = 50,000$ and $M_\infty = 0.4$. The dipole noise contribution is calculated using a frequency domain Ffocws-Williams and Hawkings formulation and contrasted for the three cases. Two-dimensional contour maps of the wall pressure spectra are also presented, revealing the dominant source strength regions for different angle of attack and frequency.

PROBLEM DESCRIPTION

In the current approach a high fidelity implicit large-eddy simulation (ILES) technique is employed to solve the full three-dimensional compressible Navier-Stokes equations in a conservative form transformed onto a generalised coordinate system. The ILES method utilises a discrete wavenumber filter with variable cut-off (normalised by grid spacing) (Kim, 2010) in order to dissipate unresolved sub-grid scales. The governing equations are as follows:

$$\frac{\partial}{\partial t} \left(\frac{\mathbf{Q}}{J} \right) + \frac{\partial}{\partial \xi_i} \left(\frac{\mathbf{E}_j}{J} \frac{\partial \xi_i}{\partial x_j} \right) = \frac{M_\infty}{Re_\infty} \frac{\partial}{\partial \xi_i} \left(\frac{\mathbf{F}_j}{J} \frac{\partial \xi_i}{\partial x_j} \right) - \frac{a_\infty}{L_c} \frac{\mathbf{S}}{J} \quad (1)$$

where a_∞ is the ambient speed of sound; and, the indices $i = 1, 2, 3$ and $j = 1, 2, 3$ denote the three dimensions. In (1), \mathbf{Q} represents the conservative variables, \mathbf{E} the convective fluxes, and \mathbf{F} the viscous and heat fluxes. The conservative variable and flux vectors are given by

$$\left. \begin{aligned} \mathbf{Q} &= [\rho, \rho u, \rho v, \rho w, \rho e_t]^T \\ \mathbf{E}_j &= [\rho u_j, (\rho u u_j + \delta_{1j} p), (\rho v u_j + \delta_{2j} p) \\ &\quad (\rho w u_j + \delta_{3j} p), (\rho e_t + p) u_j]^T \\ \mathbf{F}_j &= [0, \tau_{1j}, \tau_{2j}, \tau_{3j}, u_i \tau_{ji} + q_j]^T \end{aligned} \right\} \quad (2)$$

with the stress tensor, and the heat flux is given by

$$\tau_{ij} = \mu \left(\frac{\partial u_i}{\partial x_j} + \frac{\partial u_j}{\partial x_i} - \frac{2}{3} \delta_{ij} \frac{\partial u_k}{\partial x_k} \right) \quad q_j = \frac{\mu}{(\gamma - 1) Pr} \frac{\partial T}{\partial x_j} \quad (3)$$

where $\xi_i = \{\xi, \eta, \zeta\}$ are the generalised coordinates, $x_j = \{x, y, z\}$ are the Cartesian coordinates, and the Jacobian determinant of the coordinate transformation (from Cartesian to the body fitted) is defined as $J^{-1} = |\partial(x, y, z) / \partial(\xi, \eta, \zeta)|$. Additionally, δ_{ij} is the Kronecker delta, $u_j = \{u, v, w\}$, the total energy $e_t = p / [(\gamma - 1)\rho] + u_j u_j / 2$ and $\gamma = 1.4$ for air. Computations are carried out with dimensionless quantities. The normalisation variables are chord length (L_c), speed of sound (a_∞), and free-stream density (ρ_∞).

The governing equations given above are solved by using high-order accurate numerical methods specifically developed for aeroacoustic simulations on structured grids. The flux derivatives in space are calculated based on eight-order compact finite difference schemes at interior nodes, and sixth-order at the boundaries, based on a seven point stencil described in Kim (2007). Explicit time advancing of the numerical solution is carried out by using the classical fourth-order Runge-Kutta scheme. Numerical stability is maintained with the aforementioned sixth-order wavenumber-optimised discrete filter, utilising a cut-off wavenumber set to 0.85π (normalised by grid spacing). The computation is parallelised via domain decomposition and message passing interface (MPI) approaches. The compact finite difference schemes and filters used are implicit in space due to the inversion of pentadiagonal matrices involved, which requires a precise and efficient technique for the parallelisation in order to avoid numerical artefacts that may appear at the subdomain boundaries. A recent parallelisation approach based on quasi-disjoint matrix systems (Kim, 2013) offering super-linear scalability is used in the current methodology. Computations are carried out in the UK national supercomputer ARCHER utilising 26400 points per processor.

Domain, initial, and boundary conditions

The computational domain is shown in figure 1(a). A structured grid is used based on an H-topology, which is stretched in both the streamwise and vertical directions. The aerofoil is positioned at the centre of the grid with the origin at the mid-chord location. The geometry considered is a NACA0012 aerofoil with a sharp trailing edge (TE), and a uniform span $L_z = 0.2L_c$. A sponge layer (thickness $2L_c$) surrounds the perimeter of the domain (longitudinal and vertical boundaries) which is implemented through the source term \mathbf{S} in (1) (Kim *et al.*, 2010). The purpose of the sponge layer is to attenuate any acoustic waves in order to prevent spurious reflections at the domain boundaries

by smoothly forcing to the mean flow condition. Additionally, characteristic-based boundary conditions are implemented at the far-field boundaries (non-reflecting (Kim & Lee, 2000)) and on the aerofoil surface (non-slip (Kim & Lee, 2004)). Characteristic interface conditions are also required at the six block boundaries (see figure 1(a)) where the grid is discontinuous. In the lateral direction a periodic condition is implemented. The total grid cell count is

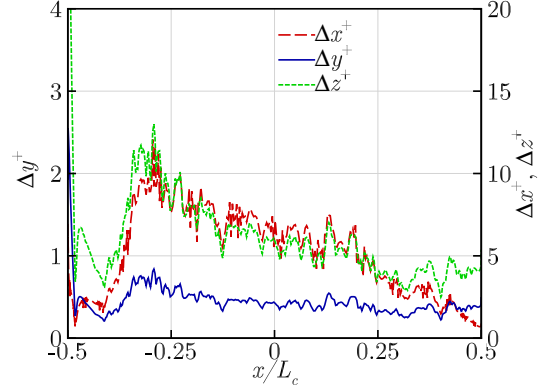


Figure 2. Spanwise averaged surface mesh sizes in wall units for $\alpha = 10^\circ$ case

$N_\xi \times N_\eta \times N_\zeta = 1200 \times 1120 \times 66 = 88,704,000$ where N_ξ , N_η and N_ζ are the number of cells in the streamwise, vertical and lateral directions, respectively. The surface mesh sizes in wall units are provided for 10° angle of attack (α) in figure 2. The wall resolution satisfies the requirements for DNS suggested by Georgiadis *et al.* (2010). In addition, a fine grid spacing is maintained on the aerofoil suction side (as shown in figure 1(b)) in order to capture the separated shear layer and transition which occurs there for higher angles of attack.

The aerofoil is in a fixed position with its chord line in the x -direction. The flow is initially ambient, and then accelerated to $u_\infty = U_\infty \cos(\alpha)$, $v_\infty = U_\infty \sin(\alpha)$, and $w_\infty = 0$ by application of a moving frame technique. The velocity is ramped up over a period of 5 time units (ta_∞ / L_c).

In figure 3 a comparison of the time averaged pressure (C_p) and skin friction (C_f) coefficients is made to the DNS data of Jones *et al.* (2008) for $\alpha = 5$ in order to validate the current numerical method. Overall there is a good match for both quantities on both suction and pressure sides. In particular there is very good agreement for the mean separation and reattachment points (at $x/L - c = -0.4$ and 0.108) shown by the C_f .

Acoustic calculations

Acoustic data in the far-field is predicted with the a frequency domain formulation of the Ffowcs-Williams and Hawkings (FW-H) Ffowcs Williams & Hawkings (1969) acoustic analogy Lockard (2000, 2002) for dipole noise.

$$p'_a H(f) = - \int_{f=0} \widehat{F}_i(\mathbf{x}_s, \omega) \frac{\partial G(\mathbf{x}_o; \mathbf{x}_s)}{\partial x_{s,i}} dS \quad (4)$$

where $\widehat{\cdot}$ is a Fourier transformed variable, $f = 0$ is the aerofoil surface, H is the heavy side step function, ω is the an-

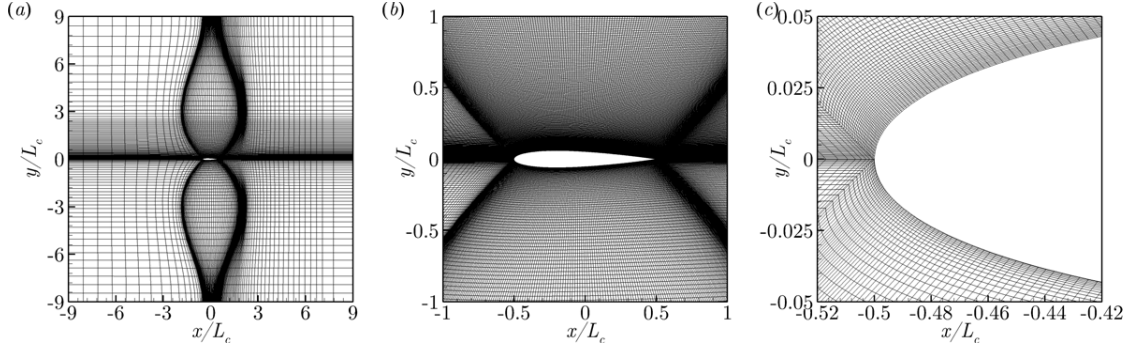


Figure 1. Computational grid. (a) full domain, 10% of points shown; (b) close up near the aerofoil, 50% of points shown. (c) close up near the aerofoil leading edge.

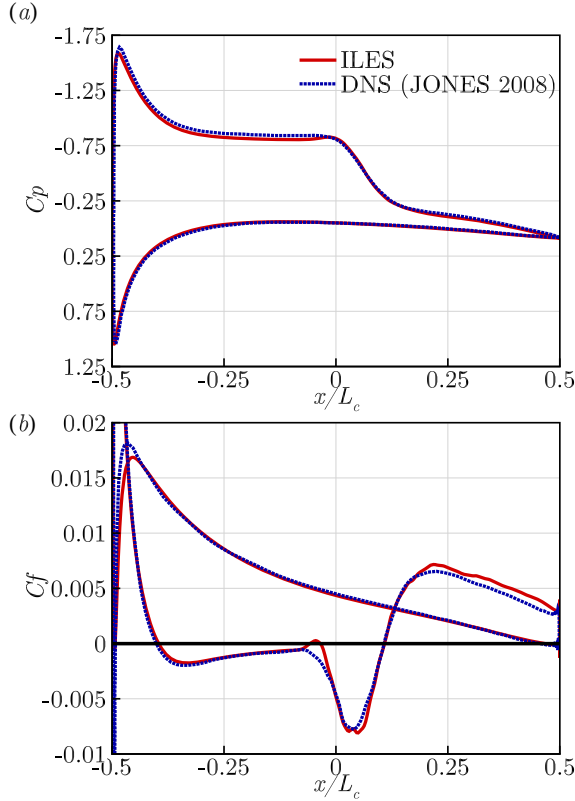


Figure 3. Time averaged pressure (a) and skin friction (b) coefficients compared to the DNS data of Jones *et al.* (2008) for $\alpha = 5^\circ$.

gular frequency, and $x_{o,i} = \{x_o, y_o, z_o\}$, $x_{s,i} = \{x_s, y_s, z_s\}$ are the observer and source coordinates. Additionally, $\hat{F}_i = \hat{p}' n_i$ (not to be confused with \mathbf{F}_j in (2)), where n_j is the outward surface normal vector. The three-dimensional greens function G is given by:

$$G(\mathbf{x}_o; \mathbf{x}_s) = -\frac{\exp(-ik[(\bar{x}^2 + \beta^2(\bar{y}^2 + \bar{z}^2))^{\frac{1}{2}} - M\bar{x}]/\beta^2)}{4\pi(\bar{x}^2 + \beta^2(\bar{y}^2 + \bar{z}^2))^{\frac{1}{2}}} \quad (5)$$

and

$$\bar{x} = (x_o - x_s) \cos(\alpha) + (y_o - y_s) \sin(\alpha) \quad (6)$$

$$\bar{y} = -(x_o - x_s) \sin(\alpha) + (y_o - y_s) \cos(\alpha) \quad (7)$$

$$\bar{z} = z_o - z_s \quad (8)$$

where $k = \omega/a_\infty$ is the wavenumber. In the current approach the surface integration is carried out over the aerofoil surface, allowing monopole contributions to be omitted from (4). Fourier transforms are calculated using the FFTW package, utilising a taper cosine window. Presently, the contribution from quadrupole sources is not considered. As shown by Wolf *et al.* (2012) quadrupoles may have a significant effect on the magnitude for medium-high frequencies. This will be investigated in the future work.

SIMULATION RESULTS

Numerical simulations are run for three angles of attack $\alpha = 5^\circ, 10^\circ$ and 15° . The CFL = 0.95, which results in an adaptive time step of approximately $\Delta t^* = 1 \times 10^{-4}$. The three cases are run for 60, 150 and 200 non-dimensional time units respectively.

In figure 4 iso-surface of Q-criterion ($Q=10$) are shown coloured by velocity magnitude, which gives an overview of the key features corresponding to each of the three cases. At $\alpha = 5^\circ$ the flow is characterised primarily by laminar separation followed by transition and reattachment as a turbulent boundary layer. For the higher angle of attack cases the aerofoil also begins to exhibit trailing edge separation. Kelvin-Helmholtz instabilities are formed in the shear layer for both 10° and 15° cases, and large scale von Kármán vortices are shed from the TE for 15° . In figure 5 the normalised stream-wise density gradient ($(\partial\rho/\partial x)L_c/\rho_\infty$) for the 5° (a) and 15° (b) cases is shown. The figure highlights significant differences in the acoustic near-field for pre- and post-stall examples. For 5° the noise radiated appears primarily dipolar. In comparison for 15° , high frequency waves are much more prominent. A significant amount of sound also appears to radiate from the wake downstream, and the leading edge shear layer, which represent possible quadrupole sources.

Dipole noise calculations

The dipole noise is calculated from the surface integral term of (4) using 1024 time samples with spacing $\Delta t^* = 5/256$. PSD is estimated using the Welch averaging technique with 3 equal segments and 50% overlap. To account for the spanwise periodic condition the FW-H calculation is performed for multiple source regions (copied and shifted in span), which are assumed to radiate independently (Wolf *et al.*, 2012). The number of source regions is selected such that the final result produces a converged solution, requiring $120L_z$. The extent to which this assumption

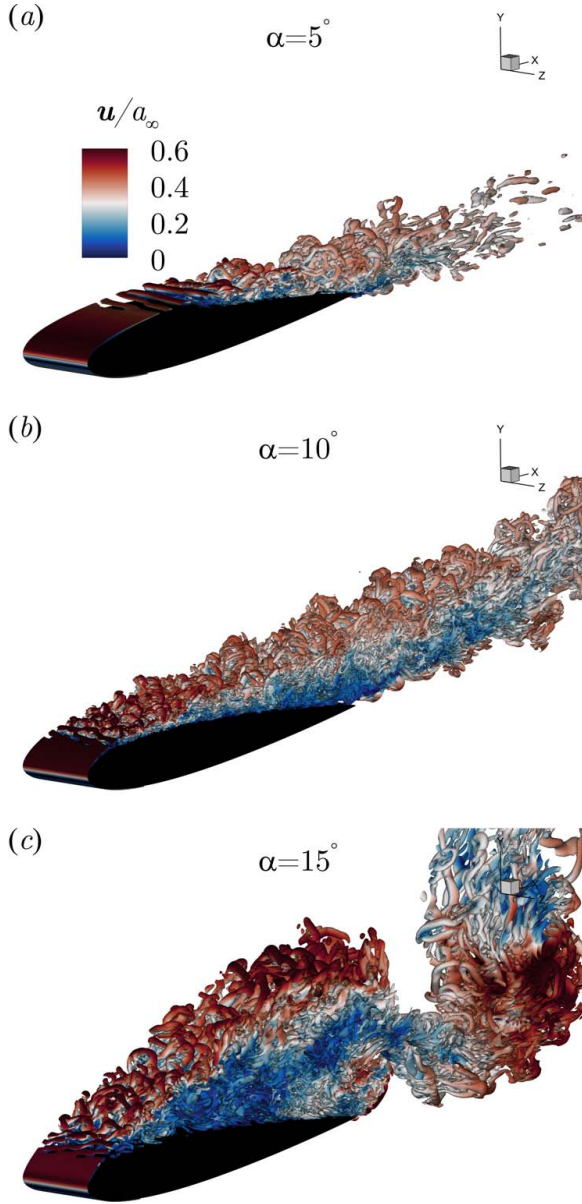


Figure 4. Iso-surface of Q-criterion ($\|\Omega_{ij}L_c/a_\infty\|^2 - \|S_{ij}L_c/a_\infty\|^2$), ($Q=10$), coloured by the magnitude of velocity for (a) $\alpha = 5^\circ$, (b) $\alpha = 10^\circ$, and (c) $\alpha = 15^\circ$.

is valid will be investigated in the future work by comparison to larger spanwise domain cases. Figure 6 shows the PSD (S_{ppa}/p_∞^2) vs Strouhal number $St = fL_c/u_\infty$, averaged over the observer angles 60° to 120° at a radius $8L_c$ from the TE.

As angle of attack is increased the low frequency noise increases considerably. The peak occurring at $St = 0.69$ for the deep stall case corresponds to the large scale vortex shedding at the TE. This contrasts with Strouhal number $St = 0.88$ observed for the same Reynolds number at 12° in the DNS data of Rodríguez *et al.* (2013) for incompressible flow. The 15° cases also exhibits less prominent tones at 1.69, 2.62, 4.18 and 5.80. For $3.4 \leq St \leq 11.0$ the pre-stall and onset-stall cases obtain a comparable level, while the post-stall cases is significantly increased in this range, often in excess of 10 dB. At higher frequencies $St > 11$, the noise level for 10° rises significantly, exceeding the level for 15° .

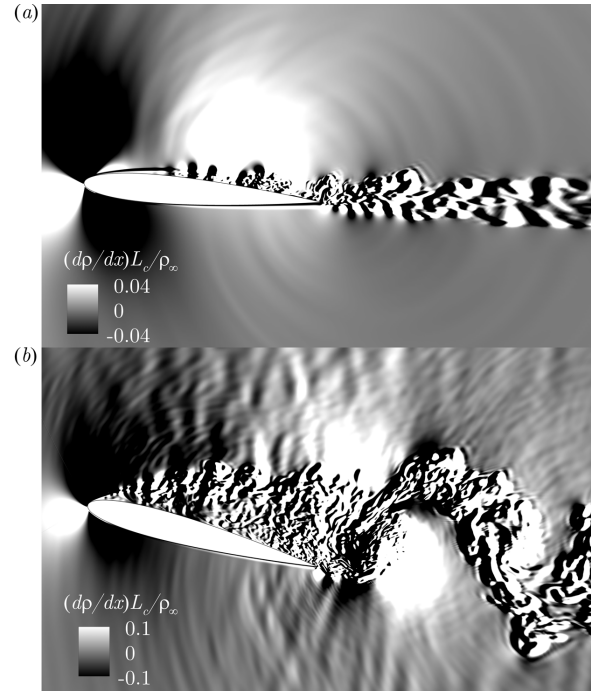


Figure 5. Stream-wise density gradient (normalised) for $\alpha = 5^\circ$ (a) and $\alpha = 15^\circ$ (b).

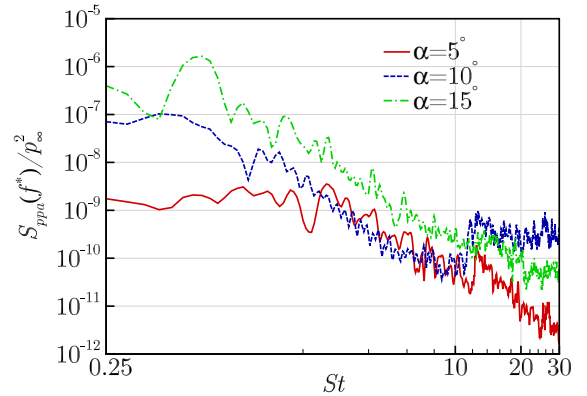


Figure 6. PSD averaged over observer angles 60° to 120° at a radius $8L_c$ from the TE obtained by the dipole component of the FW-H for three angles of attack.

A broad peak is observed for 10° at $St = 12.70$, after which the noise level remains fairly consistent. A similar peak is also observed for 5° . A peak was also observed by Wolf *et al.* (2012) at $St = 10.8$ at the same angle of attack and Mach number, which was attributed to vortex shedding near the LE.

In order to better understand the far-field noise, the source strength is considered over the aerofoil surface. Figures 6-8 show the magnitude of the Fourier transform of wall pressure jump in a logarithmic scale for $St = 0.69$, 5.80 and 12.70. Here the pressure jump is calculated by subtracting the y component of fluctuating pressure on the lower side from the upper side of the aerofoil. This directly relates to the $i = 2$ dipole term in (4). For $St = 0.69$, the 5° and 10° configurations shown a maximum source magnitude just before the reattachment point, during flow transition in the separated shear layer. Meanwhile the 15°

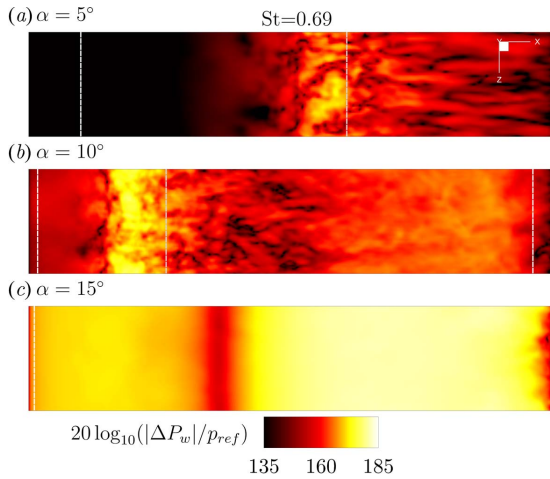


Figure 7. Contours of wall pressure jump at $St = 0.69$ in a log scale ($p_{ref} = 10^{-10} p_{\infty}$) at $\alpha = 5^\circ$ (a), $\alpha = 10^\circ$ (b), and $\alpha = 15^\circ$ (c). White and grey dashed lines represent mean separation and reattachment points.

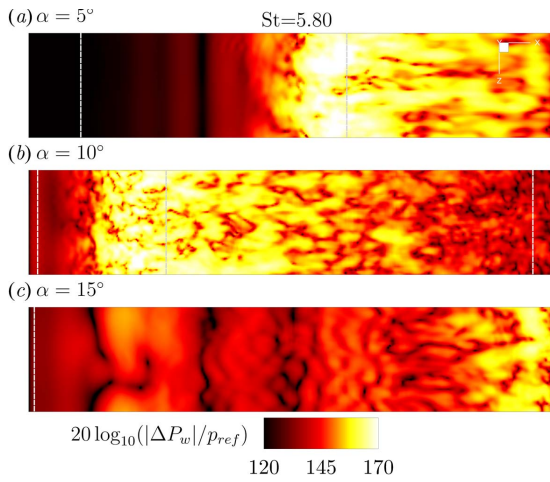


Figure 8. Contours of wall pressure jump at $St = 5.8$ in a log scale ($p_{ref} = 10^{-10} p_{\infty}$) at $\alpha = 5^\circ$ (a), $\alpha = 10^\circ$ (b), and $\alpha = 15^\circ$ (c). White and grey dashed lines represent mean separation and reattachment points.

case exhibits maximum source strength over the aft portion of the aerofoil, likely associated with low frequency von-Kármán shedding. This is also shown for the 10° case but to a lesser extent.

A similar trend is observed at $St = 5.80$ (figure 8) for the two lower angle of attacks, although the high strength source is spread over a larger area. For the full stall (15°) case, the source is mainly concentrated at the trailing edge. Surprisingly the maximum source magnitude for 15° angle of attack is noticeably smaller and more concentrated than the lower angle cases. This is despite the larger noise level observed in the far-field at the same frequency. A possible explanation for this contradiction can be obtained by also considering the phase variation of the surface. Figure 9 shows the real part of the Fourier transform of wall pressure jump at the same Strouhal number. Regions with equal magnitude which are in phase ($\phi_2 - \phi_1 = 2n\pi$) have equal sign, whereas out of phase regions ($\phi_2 - \phi_1 = n\pi$) have opposite signs. For the 5° and 10° cases there is a high level of destructive interference in the high source strength ar-

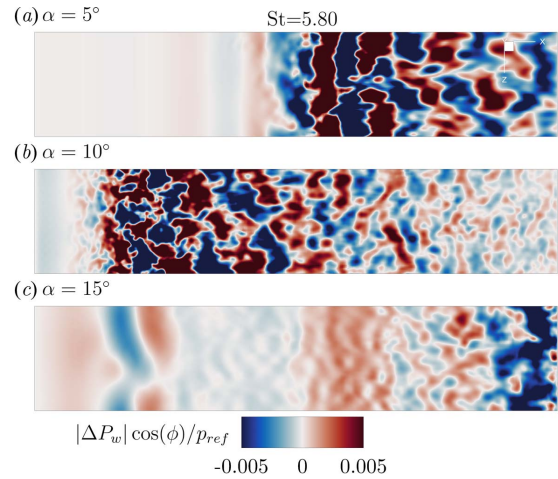


Figure 9. Real part of ΔP_w (Fourier transform of wall pressure jump) for $St = 5.8$ at $\alpha = 5^\circ$ (a), $\alpha = 10^\circ$ (b), and $\alpha = 15^\circ$ (c)

reas. Conversely, for 15° , the high strength region near the TE is almost entirely in phase. This might suggest relatively more efficient noise radiation, resulting in the peak observed in figure 6. Similar trends can also be observed from the imaginary part of the Fourier transform, which is not shown here for conciseness.

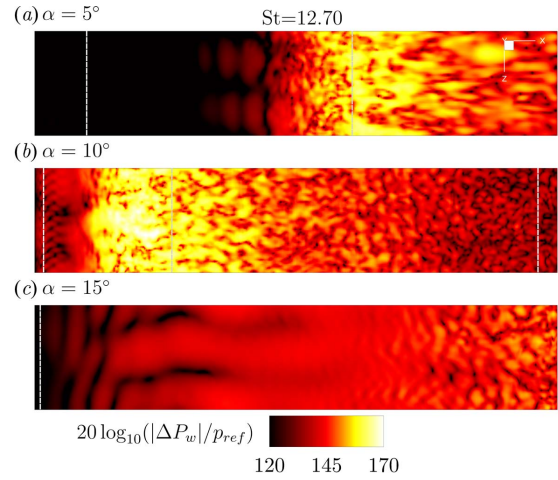


Figure 10. Contours of wall pressure jump at $St = 12.70$ in a log scale ($p_{ref} = 10^{-10} p_{\infty}$) at $\alpha = 5^\circ$ (a), $\alpha = 10^\circ$ (b), and $\alpha = 15^\circ$ (c). White and grey dashed lines represent mean separation and reattachment points.

Figure 10 shows the source magnitude for $St = 12.70$. With a few exceptions the distribution of the source magnitude is comparable to the lower Strouhal number $St = 5.80$. For 5° the location of maximum source magnitude is shifted slightly downstream, roughly coinciding with the reattachment point. Meanwhile for 10° the source becomes more concentrated in the transitional region. For 15° oblique modes are clearly visible near the leading edge and mid chord. At this frequency 10° dominates the far-field noise, while the 5° and 15° obtain a similar level. This is possibly attributed to the larger source area for the 15° case, despite weaker maximum source. The phase relationship

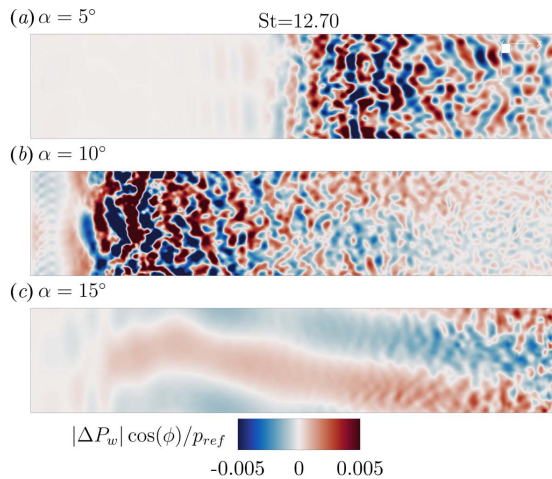


Figure 11. Real part of ΔP_w (Fourier transform of wall pressure jump) for $St = 12.70$ at $\alpha = 5^\circ$ (a), $\alpha = 10^\circ$ (b), and $\alpha = 15^\circ$ (c)

is shown in figure 11, which contains the real part of the Fourier transform at the same Strouhal number. Both 5° and 10° cases again show significant out of phase regions in the high strength source area. This indicates the higher radiated noise for the 10° case may be due to larger amplitude of wall pressure fluctuations. It is also worth pointing out how both 10° and 15° cases show noticeable large wavelength (high phase speed) variations in the spanwise direction. The result indicates that spanwise and oblique structures might play a significant role in the noise generation. This raises some questions regarding the effect of spanwise domain size on the current noise calculations, which will be investigated in the future work.

CONCLUSION & FUTURE WORK

This paper presents preliminary results of an investigation into the effects of separation and stall on aerofoil noise. High order ILES simulations of a NACA0012 aerofoil are carried out at three angles of attack 5° , 10° and 15° , at $Re_\infty = 50,000$ and $M_\infty = 0.4$. Estimates for the dipole noise contribution are calculated using a frequency domain FWH solver. It is shown how as angle of attack increased the noise greatly increases at low frequency. While at medium frequencies it remains comparable until deep stall (15°). At high frequencies, both 10° and 15° exhibit significant noise increase compared to the pre-stall case. The wall pressure spectra is also considered over the full aerofoil surface at select frequencies in order to gain additional insight into the noise generation mechanisms. It is found that generally, the 5° and 10° cases exhibit maximum source strength during transition and reattachment of the flow. The 15° case on the other hand usually shows maximum source strength towards the trailing edge. It is also suggested that phase variations on the surface can play a significant role in the radiated sound.

This paper only consider the dipole part of the radiated sound. As discussed it is possible that the quadrupole sources will also make a significant contribution to the sound amplitude at the current Mach number (Wolf *et al.*, 2012) at high frequencies. It is also important to conduct a spanwise domain sensitivity test on the current results in order to verify the three dimensional features of separated

flow are properly captured.

ACKNOWLEDGEMENT

The authors gratefully acknowledge the support of the ESPRC (Engineering and Physical Sciences Research Council) under grant (EP/R010900/1). We also acknowledge the high-performance computing facilities and services offered by the UK national supercomputer ARCHER.

REFERENCES

- Ffowcs Williams, J. E. & Hawkings, D.L. 1969 Sound generation by turbulence and surface in arbitrary motion. *Philos. Trans. R. Soc. Lond. A* **264**, 321–342.
- Georgiadis, N. J., Rizzetta, D. P. & Fureby, C. 2010 Large-eddy simulation: current capabilities, recommended practices, and future research. *AIAA J.* **48** (8), 1772–1783.
- Jones, L. E., Sandberg, R. D. & Sandham, N. D. 2008 Direct numerical simulations of forced and unforced separation bubbles on an airfoil at incidence. *J. Fluid Mech.* **602**, 175–207.
- Kim, J. W. 2007 Optimised boundary compact finite difference schemes for computational aeroacoustics. *J. Comput. Phys.* **225**, 995–1019.
- Kim, J. W. 2010 High-order compact filters with variable cut-off wavenumber and stable boundary treatment. *Comput. Fluids* **39**, 1168–1182.
- Kim, J. W. 2013 Quasi-disjoint pentadiagonal matrix systems for the parallelization of compact finite-difference schemes and filters. *J. Comput. Phys.* **241**, 168–194.
- Kim, J. W., Lau, A. S. H. & Sandham, N. D. 2010 Proposed boundary conditions for gust-airfoil interaction noise. *AIAA J.* **48** (11), 2705–2709.
- Kim, J. W. & Lee, D. J. 2000 Generalized characteristic boundary conditions for computational aeroacoustics. *AIAA J.* **38** (11), 2040–2049.
- Kim, J. W. & Lee, D. J. 2004 Generalized characteristic boundary conditions for computational aeroacoustics, part 2. *AIAA J.* **42** (1), 47–55.
- Lacagnina, G., Chaitanya, P., Berk, T. Joseph, P., Hasheminejad, S. M., Stalnov, O., Chong, T. P. & Ganapathisubramani, B. 2018 Effect of leading edge serrations in reducing aerofoil noise near stall conditions. In *24th AIAA/CEAS Aeroacoustics Conference. AIAA Paper* 2018-3285.
- Lockard, D. P. 2000 An efficient, two-dimensional implementation of the Ffowcs Williams and Hawkings equation. *J. Sound Vib.* **229** (4), 897–911.
- Lockard, D. P. 2002 A comparison of Ffowcs Williams-Hawkings solvers for airframe noise applications. In *8th AIAA/CEAS Aeroacoustics Conference. AIAA Paper* 2002-2580.
- Moreau, S., Roger, M. & Christophe, J. 2009 Flow features and self-noise of airfoils near stall or in stall. In *15th AIAA/CEAS Aeroacoustics Conference. AIAA Paper* 2009-3198.
- Rodríguez, I., Lehmkuhl, O., Borrell, R. & Oliva, A. 2013 Direct numerical simulation of a NACA0012 in full stall. *Int. J. Heat Fluid Fl.* **43**, 194–203.
- Wolf, W. R., Azevedo, J. L. F. & Lele, S. K. 2012 Convective effects and the role of quadrupole sources for aerofoil aeroacoustics. *J. Fluid Mech.* **708**, 502–538.